Nanoscale

Accepted Manuscript

This article can be cited before page numbers have been issued, to do this please use: F. Li, X. Lv, J. Gu, K. Tu, J. Gong, P. Jin and Z. Chen, *Nanoscale*, 2019, DOI: 10.1039/C9NR07263B.

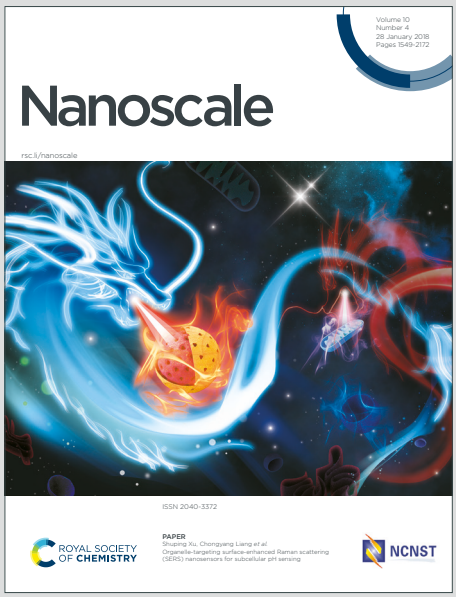

ROYAL SOCIETY OF CHEMISTRY

rsc.li/nanoscale

Semiconducting SN_2 Monolayer with Three-Dimensional Auxetic Properties: A Global Minimum with Tetracoordinated Sulfurs

Fengyu Li,[a,#]* Xiaodong Lv,[a,#] Jinxing Gu,[b] Kaixiong Tu,[b] Jian Gong,[a] Peng Jin,[c,]* Zhongfang Chen[b,]*

[a] *School of Physical Science and Technology, Inner Mongolia University, Hohhot, 010021, China*

[b] *Department of Chemistry, The Institute for Functional Nanomaterials, University of Puerto Rico, Rio Piedras Campus, San Juan, PR 00931, USA*

[c] *School of Materials Science and Engineering, Hebei University of Technology, Tianjin 300130, China.*

*Corresponding Author: fengyuli@imu.edu.cn (FL); china.peng.jin@gmail.com (PJ); zhongfangchen@gmail.com (ZC)

[#] Equal contribution to this work.

View Article Online
DOI: 10.1039/C9NR07263B

Abstract

Designing new two-dimensional (2D) materials, exploring their unique properties and diverse potential applications are of paramount importance to condensed matter physics and materials science. In this work, we predicted a novel 2D SN_2 monolayer (*S*-SN_2) by means of density functional theory (DFT) computations. In the *S*-SN_2 monolayer, each S atom is tetracoordinated with four N atoms, and each N atom bridges two S atoms, thus forming a tri-sublayer structure with square lattice. The monolayer exhibits good stability, as demonstrated by the moderate cohesive energy, all positive phonon modes, and the structural integrity maintained through 10 ps molecular dynamics simulations up to 1000 K. It is an indirect-bandgap semiconductor with high hole mobility, and the bandgap can be tuned by changing the thickness and external strains (the indirect-bandgap to direct-bandgap transition occurs when the biaxial tensile strain reaches 4%). Significantly, it has large Young's modulus and three-dimensional auxetic properties (both in-plane and out-of-plane negative Poisson's ratios). Therefore, the *S*-SN_2 monolayer holds great potential applications in electronics, photoelectronics and mechanics.

Keywords: two-dimensional materials, density functional theory, stability, strain, electronic properties, auxetic properties, optical properties, tetracoordinated sulfur

View Article Online
DOI: 10.1039/C9NR07263B

1. Introduction

Binary sulfur-nitrogen molecules with different chemical compositions and configurations have been investigated for years,[1–3] however, most of them could only exist at low temperatures. For example, dinitrogen sulfide (N_2S) will decompose into N_2 and S_2 when the temperature is higher than 160 K. The disulfur nitride could be produced in a microwave-discharged argon/nitrogen/sulfur steam and trapped in solid argon at 12 K.[4] The reported sulfur-nitrogen crystals are mainly composed of ring clusters [5–8] or SN chains.[9,10] Recently, Li *et al*. performed a systematic computational study on the structural, electronic and bonding properties of sulfur nitrides, and predicted four high-pressure phases of SN_x.[11] Among them, the SN_2 with orthorhombic *Pnnm* space group is a direct-bandgap semiconductor (bandgap: 0.66 eV) at 60 GPa, and quite recently, the proposed SN_2 solid was successfully synthesized above 64 GPa.[12]

In addition to the three-dimensional (3D) binary sulfur nitrides, their 2D counterparts were also predicted theoretically. Very recently, Chen's group proposed a dynamically and thermally stable trisulfur dinitride (S_3N_2) 2D crystal, whose indirect band gap is as wide as 3.92 eV, and could be further tuned by forming multilayers, nanoribbons and nanotubes.[13] Based on the structure of 1*T*-MoS_2, Lin *et al*. theoretically designed a 1*T*-SN_2 single-layer.[14] 1*T*-SN_2 was computed to be an indirect-bandgap semiconductor with wide bandgap (2.83 eV), and the bandgap could be narrowed by external biaxial stretching. The 1*T*-SN_2 monolayer has dynamical stability, however, its thermal and mechanical stabilities are to be determined, its bandgaps under uniaxial strain and the thickness of multilayers are yet unknown. More importantly, is 1*T*-SN_2 monolayer the lowest-energy configuration of the 2D

View Article Online
DOI: 10.1039/C9NR07263B

SN_2 crystals? If not, what is the structure of the most stable SN_2 monolayer and what intriguing properties will it possess?

To address the above issues, we performed a global minimum search for SN_2 in the 2D space, and a novel *S*-SN_2 monolayer with tetracoordinated S atoms was reached. The *S*-SN_2 monolayer is extraordinarily stable and is an indirect-bandgap semiconductor with a slightly narrow bandgap of 2.79 eV compared to that of the 1*T*-SN_2 (2.89 eV). Significantly, it features in-plane and out-of-plane negative Poisson's ratios, and is thus a potential 3D auxetic material.

2. Computational Methods

All spin-polarized density functional theory (DFT) computations were carried out by using the generalized gradient approximation (GGA) in the form of the Perdew-Burke-Ernzerhof exchange-correlation functional (PBE).[15] Projector augmented wave (PAW) method [16] was used as implemented in the Vienna ab initio simulation package (VASP) code.[17] The PBE-D2 approach [18] with dispersion energy correction was used for the geometry optimization of the bulk and few layers. The Monkhorst-Pack scheme [19] of 9×9×1 *k*-points mesh was applied for the unit cell geometry optimizations, while a larger grid (25×25×1) was used for the electronic structure computations. The HSE06 functional [20] was utilized to obtain more accurate band structures. The dynamic energy cutoff for the plane-wave basis set was set to be 600 eV. During the geometry optimizations, both the lattice constants *a* and *b*, and the atomic positions were fully relaxed until the atomic forces on the atoms were less than 10^{-5} eV/Å and the total energy change was less than 10^{-6} eV. To avoid interactions between periodic images, a large vacuum region of ~15 Å was applied to the perpendicular direction of the 2D layer.

View Article Online
DOI: 10.1039/C9NR07263B

First-principles molecular dynamics (FPMD) simulations were performed to assess the thermal stability of the 2D materials at the PBE level with the temperature controlled by the Nosé-Hoover method.[21] The initial configurations were annealed at different temperatures. At each temperature, the MD simulation in an NVT canonical ensemble lasted for 10 ps with a time step of 0.5 fs.

The particle-swarm optimization (PSO) multidimensional method, as implemented in the CALYPSO code,[22] was employed to search for the low-energy structures. In our PSO simulations, the population size was set at 30, the number of generations was maintained at 50. The unit cells contained 3, 6, 9 and 12 total atoms. The structure relaxations employed the PBE functional, as implemented in VASP software.

3. Results and Discussion

3.1. Geometric Properties of the *S*-SN_2 Monolayer

Our global minimum search for SN_2 in the 2D space revealed that a novel square lattice structure with tetracoordinate S atoms (Fig. 1a) has the lowest energy. The unit cell of this SN_2 monolayer consists of one S atom and two N atoms. The optimized structure of the monolayer has the symmetry of $P\bar{4}M2$ with the square lattice of 2.63 Å, in which each S atom is tetracoordinated with four N atoms, and each N atom bridges two S atoms, thus forming a tri-sublayer structure (Fig. 1a). To differentiate this new structure from the previous reported 1*T*-SN_2,[14] we denote this new monolayer as *S*-SN_2 considering its square lattice.

The N–S bonds (*d*) of *S*-SN_2 have the uniform length of 1.62 Å, and the layer thickness (*h*) is 1.88 Å, both shorter than those of the previously proposed 1*T*-SN_2 monolayer (the *d* and *h* values are 1.80 and 1.90 Å, respectively, at the same level of

View Article Online
DOI: 10.1039/C9NR07263B

theory). Note that structurally the *S*-SN_2 monolayer well resembles the recently proposed monolayers of Tetra-MoN_2 [23] and CO_2,[24] and the orthorhombic SN_2 (*Pnnm*) predicted by Li *et al*. can be considered as its bulk precursor.[11] In the *Pnnm*-SN_2 solid, the S atoms are hexa-coordinated and N atoms are tri-coordinated, the (0 0 1) slab can be viewed as the twisted *S*-SN_2 monolayer.

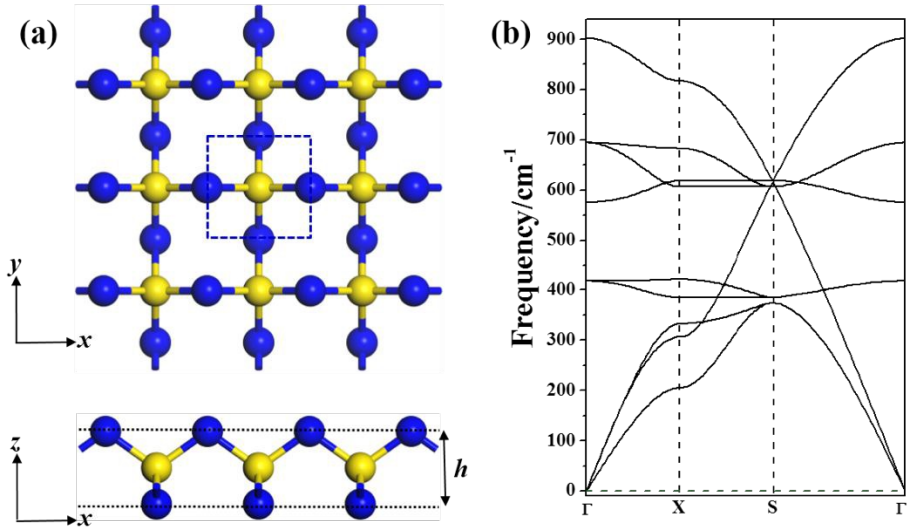

Fig. 1 The *S*-SN_2 monolayer: (a) Optimized structure from top and side views (a 3×3×1 supercell, the unit cell is highlighted by the blue dashed square), blue and yellow balls denote N and S atoms, respectively; (b) Computed phonon spectrum.

Note that the sulfur atoms adopt the hexacoordinated and tetracoordinated states in the 1*T*-SN_2 and *S*-SN_2 monolayers, respectively. The hexacoordination of S was also realized in the dimeric N-Chloroiminosulfur tetrafluoride.[25] However, the tetracoordination of S, which was regarded to be only found in intermediates because of the strain,[26] was barely obtained in experiment.[27] It was recognized that usually electron-withdrawing groups such as F, O, and N are needed to stabilize the hypervalent state of sulfur.[28] Thus, we expect that the 1*T*/*S*-SN_2 monolayer containing

View Article Online
DOI: 10.1039/C9NR07263B

the hexa/tetracoordinated S moiety is stabilized by the N atoms, each of which withdraws 0.19/0.23 e^- from S according to our Hirshfeld charge analysis.[29]

3.2. Stability of the S-SN_2 Monolayer

The intriguing structure of *S*-SN_2 monolayer inspired us to further examine its stability. Firstly, we computed its cohesive energy (E_{coh}), which is obtained by $E_{coh} = (nE_N + mE_S - E_{SN2})/(n+m)$, where E_N, E_S and E_{SN2} are the total energies of a single N atom, a single S atom, and the SN_2 monolayer, respectively. n and m are the number of N and S atoms in the supercell. According this definition, a material with a more positive E_{coh} value has a higher thermodynamic stability. The cohesive energy of the *S*-SN_2 monolayer is 3.24 eV/atom, larger than those of the 1*T*-SN_2 monolayer (3.08 eV/atom) and the 3D SN_2 crystal (2.68 eV/atom at 60 GPa),[11] but smaller than the E_{coh} value (3.45 eV/atom) of the cage-like S_4N_4 molecular crystal,[30] the starting material for various synthetic routes in sulfur-nitrogen chemistry. In comparison, the cohesive energies of the experimentally realized 2D silicene [31,32] and phosphorene [33,34] are 3.54 and 3.48 eV/atom, respectively, at the same level of theory. The rather favorable cohesive energy of the *S*-SN_2 monolayer ensures that it has a strongly connected network, and is very promising to be synthesized.

Secondly, we confirmed that the *S*-SN_2 monolayer is also dynamically stable, as demonstrated by the real frequency values in the phonon spectrum (Fig. 1b). The highest frequency is 900 cm^{-1}, which is ~50 cm^{-1} higher than that of 1*T*-SN_2,[14] and also higher than those of silicene (580 cm^{-1}) [35] and phosephorene (456 cm^{-1}),[36] indicating its remarkable dynamic stability.

Thirdly, we examined its thermal stability by performing first-principles molecular dynamics (FPMD) simulations with a 5×5 supercell. Our simulations at

View Article Online
DOI: 10.1039/C9NR07263B

300 K, 500 K, 1000 K, and 1500 K showed that the *S*-SN_2 monolayer maintained its structural integrity throughout the 10 ps FPMD simulation up to 1000 K, but seriously distorted at 1500 K (Fig. S1). The slightly distorted structure after the simulation at 1000 K can recover the initial configuration of *S*-SN_2 monolayer upon full atomic relaxation. In comparison, the reported 1*T*-SN_2 monolayer can also maintain the structural integrity up to 1000 K in our FPMD simulations (Fig. S2), while the proposed S_3N_2 monolayer would dissociate into multiple S-N chains and clusters at the same high temperature.[13]

The above results demonstrated that the *S*-SN_2 monolayer is rather stable, and is expected to be experimentally feasible. Reminiscing the aromaticity in the ring structure of S_2N_2 and other sulfur-nitrogen molecules,[3,37] the high stability of the *S*-SN_2 monolayer raised another question: is the *S*-SN_2 monolayer also aromaticity? To address this question, we examined the chemical bonding patterns of the *S*-SN_2 monolayer by using the solid state adaptive natural density partitioning (SSAdNDP) method.[38] The SSAdNDP results suggest that besides the two *sp*-orbital lone-pairs and two *p*-orbital lone-pairs on N atoms, there are four two-center-two-electron bonds between N and S in the unitcell of *S*-SN_2 monolayer (Fig. S3). As a result, the *S*-SN_2 monolayer is not aromatic. Nevertheless, the sp^2(N)-sp^3(S) hybridization bonds lead to robust connection between the N and S atoms, and thus result in the pronouncing stability of 2D N−S network.

3.3. Electronic and Optical Properties of the S-SN_2 Monolayer.

We further investigated the electronic properties of *S*-SN_2 monolayer at the HSE06 level of theory. Similar to the 1*T*-SN_2 monolayer, which has an indirect bandgap (E_g) of 2.89 eV according to our calculations (2.83 eV in the literature [14]),

View Article Online
DOI: 10.1039/C9NR07263B

the *S*-SN_2 monolayer is also an indirect-gap semiconductor with the bandgap of 2.79 eV (Fig. 2a). The valence band maxima (VBM) are mainly composed of *p* orbitals of nitrogen atoms, similar to the case of Tetra-MoN_2,[23a] while the conduction band minima (CBM) consist of both S-*p* and N-*p* states (Fig.s 2b,c).

To gain further insights into the chemical bonding of the *S*-SN_2 monolayer, we examined the electron localization function (ELF), as visualized in Fig. 2d. Since the S atoms donate electrons to N atoms as suggested by the Hirshfeld charge analysis (0.23 e^- per N atom), the electron density around N atoms is rather localized with high ELF values. The electrons localized between S and N atoms show some deviation from the bond center, indicating the nature of polar covalent bonding, which partially contributes to the high thermal stability of the *S*-SN_2 monolayer.

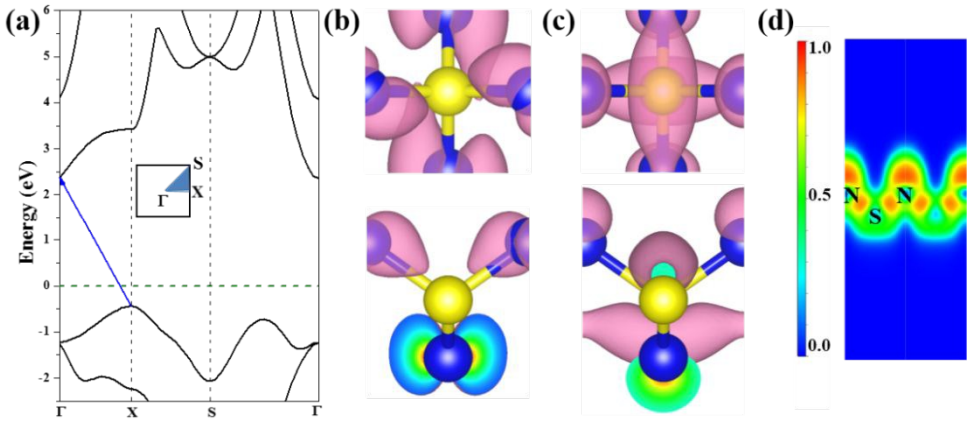

Fig. 2 The *S*-SN_2 monolayer: (a) Band structure (the Fermi energy was set to be zero and denoted by the green dashed line), (b) spatial distributions of wave functions of VBM and (c) CBM from the top and side views (isovalue: 0.02 eÅ^{-3}); (d) ELF map sliced perpendicular to the 2D plane, red (ELF = 1) and blue (ELF = 0) indicate accumulated and vanishing electron density, respectively.

View Article Online
DOI: 10.1039/C9NR07263B

Since applying external strain is an effective way to engineer the band structures of 2D nanomaterials, we studied the effect of uniaxial and biaxial (tensile and compressive) strains (η) along x and y directions on the band structure of the S-SN_2 monolayer, in comparison with the 1T-SN_2 monolayer. During the uniaxial and biaxial strains, the dynamic stabilities of the S-SN_2 monolayer could be reserved with η in the range of $-2\% \leq \eta \leq 8\%$ and $-2\% \leq \eta \leq 9\%$, respectively. When the uniaxial (biaxial) strain of 9% (10%) or larger is imposed to the S-SN_2 monolayer, imaginary frequencies will appear in the calculated phonon spectra (Fig. S4), indicating that the dynamic instability of the monolayer under such extreme strains.

When the uniaxial strains (either compression or stretching) are applied to the S-SN_2 monolayer, the bandgap decreases compared to that of the equilibrium structure (Fig. 3a). In particular, the uniaxial tensile strain could effectively decrease the bandgap: the value is reduced from the original 2.79 eV to 1.18 eV under uniaxial tensile of 8% (Fig. S5). The uniaxial strains destroy the symmetry in the reciprocal space of the S-SN_2 monolayer, and the CBM shifts down under both compression and expansion strains along the x-direction (remaining at Γ point for $-2\% \leq \eta \leq 7\%$, but switching to Y point for $\eta = 8\%$), while the VBM oscillates around the X point, as a result, the bandgap is decreased regarding to the pristine E_g.

In comparison, we examined the effect of uniaxial strain on the electronic structure of the 1T-SN_2 monolayer. Interestingly, under the strain modulation, the 1T-SN_2 monolayer remains the indirect-gap semiconducting nature. The band gap of 1T-SN_2 exhibits a quasi-linear relation with the uniaxial strain in either x (armchair) or y (zigzag) direction (Fig. S5): the band gap increases (decreases) monotonically with the tensile (compressive) strain along x direction, and the gap change is in a relative small range (2.82~2.96 eV) when the strain of –2% to 2% is applied; however, along

View Article Online
DOI: 10.1039/C9NR07263B

y direction, the band gap decreases (increases) in a more pronounced manner with the tensile (compressive) strain. When the *y*-axial tensile strain is as large as 5%, the gap value reduces to 2.44 eV from 2.89 eV of the pristine monolayer; when the –2% compressive strain is imposed along the *y* direction, the gap is enlarged to 3.14 eV.

When applying biaxial strains to the *S*-SN_2 monolayer in the range of –2%~3%, the bandgap increases almost linearly with increasing the strain (2.73~2.82 eV). When the tensile strain is even larger, at the external tensile of 4%, the bandgap drops from the linear relation, and the indirect-gap to direct-gap transition occurs (bandgap of 2.65 eV, Fig. S5). Further increasing the strain continues to narrow the bandgap, but transits to indirect bandgap again, since the VBM moves from X/Y *k*-point for η = 4% to the value between X and Γ *k*-points for larger stretches, and under the biaxial tensile of 9%, the indirect bandgap of the *S*-SN_2 monolayer is 1.01 eV. In comparison, the band gap of the 1*T*-SN_2 monolayer decreases monotonically from ~4.3 to ~0.6 eV as the biaxial strain increases from −10% to 10%.[14]

Overall, the strain-tailored band structure of the *S*-SN_2 monolayer can be contributed to the variation of the N−S bonds: the uniaxial or biaxial stretching weakens the N−S bonds, and as a result the CBM moves to lower energies and the bandgap was narrowed (Fig. S6), which is in line with previous DFT finding that the strain effect on the band structures of boron nitride monolayers originates from the B−N bonding.[39]

View Article Online
DOI: 10.1039/C9NR07263B

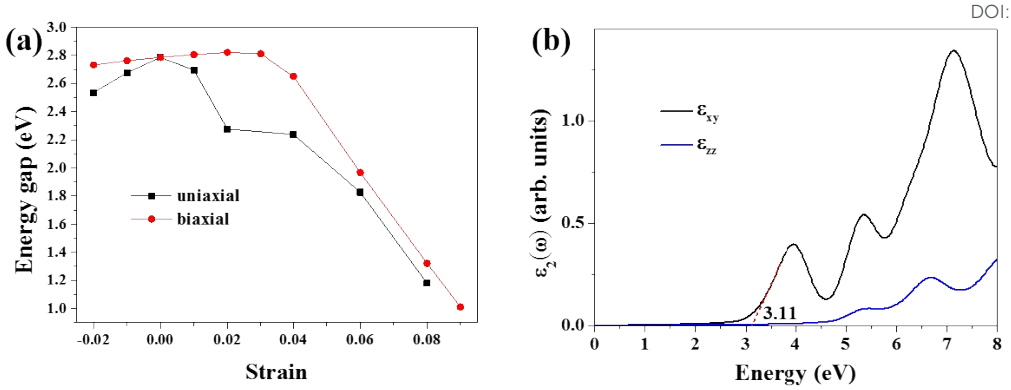

Fig. 3 (a) The HSE06 band gap as a function of the external strains for the *S*-SN_2 monolayer. (b) The imaginary dielectric constants (The red dashed line denotes an approximate linear fitting for estimating the band edge of the first adsorption peak).

Note that the *S*-SN_2 monolayer is an indirect-gap semiconductor with the VBM and CBM located at the X and Γ points, respectively. This is beneficial to restrain the recombination of the photo-activated electron-hole pairs.[40] Thus, we also investigated the optical adsorption property of the *S*-SN_2 monolayer by computing the imaginary parts of the dielectric function $\varepsilon_2(\omega)$. As shown in Fig. 3b, *S*-SN_2 exhibits adsorption starting at ~2.2 eV, and the optical gap (estimated by linear fitting of the first adsorption peak) is 3.11 eV, much smaller than that of 1*T*-SN_2 (3.86 eV, Fig. S7). Therefore, the *S*-SN_2 monolayer might be used as the visible-light-driven photocatalysts.

3.4. Carrier Mobility of the *S*-SN_2 Monolayer

We then systematically investigated the carrier mobility of the *S*-SN_2 monolayer to better understand its electronic properties using the deformation potential (DP) theory,[41] which has been extensively applied to evaluate the carrier mobility of various 2D materials,[34,42–49] and is derived from the following expression:

View Article Online
DOI: 10.1039/C9NR07263B

$$\mu = \frac{2e\hbar^3 C}{3k_B T|m^*|^2 E_1^2}$$

where, $\hbar$ is the reduced Planck constant, k_B is the Boltzmann constant, T is the temperature (the room temperature 300 K was adopted in our study), m^* is the effective mass in the transport direction, E_1 and C are the DP constant and the in-plane stiffness, respectively. E_1 signifies the shift of the band edges E_{edge} (VBM and CBM) induced by the strain δ ($\delta = \Delta a/a_o$, Δa and a_o are the variation and equilibrium lattice lengths, respectively), with the form of $E_1 = \partial E_{edg}/\partial\delta$. The in-plane stiffness can be determined by $C = (\partial^2 E/\partial\delta^2)/S_o$, where E is the total energy of the supercell, δ is the applied uniaxial strain, and S_o is the area of the equilibrium supercell.

The carrier mobility of the *S*-SN_2 monolayer was evaluated along the *x* and *y* directions (Fig. 1a). The details of computing the in-plane stiffness *C* and the DP constant E_1 are given in Fig. S6 and Table 1. The *S*-SN_2 monolayer shows very high hole mobility of 1.16×10^3 $cm^2\ V^{-1}\ s^{-1}$ for holes along both *x* and *y* directions, much higher than that of MoS_2 (200 $cm^2\ V^{-1}\ s^{-1}$);[46] while the electron mobility (0.16×10^3 $cm^2\ V^{-1}\ s^{-1}$) is comparable to those of black phosphorene (0.08×10^3~1.14×10^3 $cm^2\ V^{-1}\ s^{-1}$).[45] In comparison, the 1*T*-SN_2 monolayer has anisotropic carrier mobility along the *x* and *y* directions (Fig. S7,8), and the electron mobility (~2×10^3 $cm^2\ V^{-1}\ s^{-1}$) is higher than those of holes (0.24×10^3 $cm^2\ V^{-1}\ s^{-1}$ and 0.05×10^3 $cm^2\ V^{-1}\ s^{-1}$ in *x* and *y* directions, respectively) in either direction, which is different from *S*-SN_2, MoS_2 and phosphorene with more mobile holes.[45,46] The anisotropy of electron and hole

View Article Online
DOI: 10.1039/C9NR07263B

mobilities was found in many 2D materials, such as the group 15 monolayers,[50] the methyl-terminated germanene,[51] 8B-*Pmmn* borophene/borophane,[52] and MXenes.[53]

Table 1 The calculated effective mass m^*, DP constant E_1, in-plane stiffness C, and carrier mobility m of the S-SN_2 and 1T-SN_2 (in italic) monolayers along x and y directions.

Carrier type	m^* x/m_0	m^* y/m_0	$\lvert E_{1x} \rvert$ (eV)	$\lvert E_{1y} \rvert$ (eV)	C_x (J m^{-2})	C_y (J m^{-2})	μ_x (10^3 cm^2 V^{-1} s^{-1})	μ_y (10^3 cm^2 V^{-1} s^{-1})
electron	0.47		10.43		279.82		0.16	
	0.80	*0.28*	*1.79*	*4.76*	*242.20*	*242.20*	*1.67*	*1.87*
hole	–2.46		0.75		279.82		1.16	
	–0.88	*–1.36*	*4.26*	*6.33*	*242.20*	*242.20*	*0.24*	*0.05*

3.5. Mechanical Properties of the S-SN_2 Monolayer

Besides the electronic properties, we also investigated the mechanical properties of the S-SN_2 monolayer by examining the elastic constants. The computed elastic constants of graphene are $C_{11} = C_{22} = 351.77$ N/m and $C_{12} = C_{21} = 60.13$ N/m, which are in good agreement with previous experimental measurements [54] and computational results.[55] For the S-SN_2 monolayer, the computed elastic constants are $C_{11} = C_{22} = 282.89$ N/m, $C_{12} = C_{21} = -29.50$ N/m, and $C_{44} = 10.34$ N/m. Based on the mechanical stability criteria ($C_{11}C_{22} - C_{12}^2 > 0$, $C_{44} > 0$),[56] the S-SN_2 monolayer is mechanically stable and isotropic: it has a negative in-plane Poisson's ratio of –0.104 (C_{12}/C_{11}) for both x and y directions, and a high in-plane Young's modulus (($C_{11}C_{22} - C_{12}C_{21}$)/$C_{22}$) of 279.82 N/m, larger than those of 1T-SN_2 (242.20 N/m) and MoS_2 (124.06 N/m) monolayers at the same level of theory.

To confirm the unusual negative Poisson's ratio (NPR), we examined a series of uniaxial tensile strains as illustrated in Fig. 4. When elongating along x direction by δ_x

View Article Online
DOI: 10.1039/C9NR07263B

($1\% \leq \delta_x \leq 5\%$) of the *S*-$SN_2$ monolayer, expansions in both the in-plane *y* direction and the out-of-plane *z* direction were found as indicated by the positive resultant strains along *y* and *z* directions (δ_y and δ_z). More specifically, the resultant strain δ_y increases monotonically from 0.85% to 1.34% when the applied tensile δ_x enhances from 1% to 6%; while the resultant δ_z decreases from 1.46% to 0.11% when δ_x is increased from 1% to 5%, and the δ_z value decreases to a negative value of −0.33% when δ_x reaches 6%. The coexistence of the out-of-plane NPR and the in-plane NPR suggests that the *S*-SN_2 monolayer is new family member of 2D monolayers with 3D auxetic properties following the just predicted S_3N_2 monolayers with α-heart structure (whose in-plane NPR is −0.026, much smaller than the corresponding value –0.104 of the *S*-SN_2).[57]

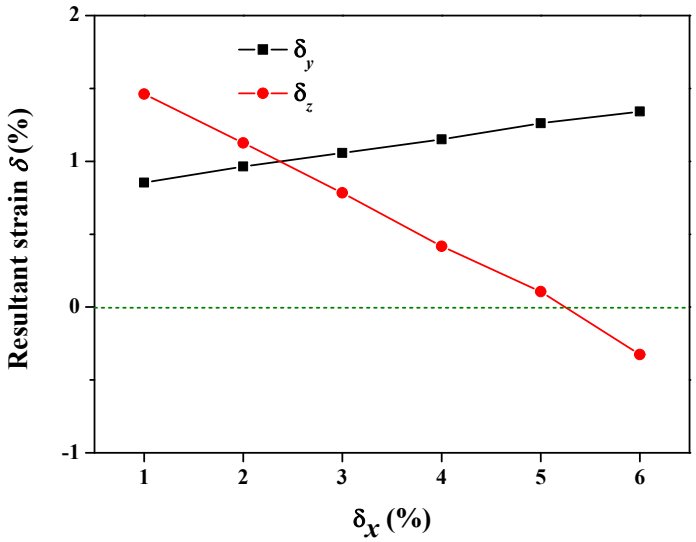

Fig. 4 Mechanical response of the *S*-SN_2 monolayer under uniaxial tensile strain along *x* direction.

3.6. The *S*-SN_2 Bilayers

View Article Online
DOI: 10.1039/C9NR07263B

Thickness and stacking pattern were also examined to get further insights into the electronic properties of *S*-SN_2, since they can affect the properties of 2D materials.[40c,58] Two possible stacking patterns of *S*-SN_2 bilayer, namely AA and AB stackings, were considered (Fig. S9). In comparison, we also examined the stacking patters of the 1*T*-SN_2 bilayer (four patterns, AA, AA', AB, and AB', Fig. S10).

The interlayer distances (4.55 and 4.81 Å for AA and AB stacking, respectively) of the *S*-SN_2 bilayers are larger than those of 1*T*-SN_2 bilayers (2.95~3.07 Å, Table S1). The binding energy (E_b) of the SN_2 bilayer in different stacking configurations is calculated via $E_b = (2 \times E_{monolayer} - E_{bilayer})/2$, where $E_{monolayer}$ and $E_{bilayer}$ are the total energies of the SN_2 monolayer and bilayer, respectively. The binding energies of the *S*-SN_2 bilayers (0.30 and 0.29 eV for AA and AB stacking, respectively) are comparable to or slightly higher than those of 1*T*-SN_2 bilayers (0.28~0.29 eV, Table S1).

As expected, the bandgaps of *S*-SN_2 bilayer in AA and AB stacking configurations are respectively reduced to 2.64 and 2.60 eV (Fig. S9) compared to that of the monolayer (2.79 eV), the *S*-SN_2 bulk in the AA stacking remains being indirect semiconducting but with a further reduced band gap of 2.58 eV.

Similarly, the indirect band width of 1*T*-SN_2 bilayer was narrowed compared to that of monolayer: 2.76 and 2.69 eV for the AB and AA stacking, respectively. Since the band gap is more sensitive in the AA stacking pattern and the stability of AA stacking is very close to the AB stacking for 1*T*-SN_2 bilayer, we further computed the electronic structures of the 1*T*-SN_2 trilayer and tetralayer in AA stacking (Fig. S11). The band gap turns to be 2.59 and 2.54 eV, respectively, and the 1*T*-SN_2 bulk in AA stacking has an indirect bandgap of 2.28 eV.

View Article Online
DOI: 10.1039/C9NR07263B

4. Conclusion

In summary, we predicted a new phase of SN_2 monolayer, namely *S*-SN_2, by using first-principles calculations combined with the particle-swarm optimization method. Its structure belongs to space group $P\bar{4}M2$ and features the unusual tetracoordinated S. The moderate cohesive energy, absence of imaginary modes in phonon spectrum, and structural integrity through 10 ps FPMD simulations up to 1000 K indicate the high stability of the *S*-SN_2 monolayer. The *S*-SN_2 monolayer is an indirect-bandgap semiconductor with high hole mobilities, and shows adsorption in the visual-light region. The bandgap of the *S*-SN_2 monolayer can be further tuned by thickness and external strains, and an indirect-direct bandgap transition could be induced under the biaxial tensile strain. Moreover, it has large Young's modulus, and the coexistence of out-of-plane and in-plane negative Poisson's ratios renders the *S*-SN_2 monolayer 3D auxetic properties. Therefore, the *S*-SN_2 monolayer is expected to have wide applications in electronics, photoelectronics, and mechanics. Especially, we are calling for more efforts in developing 2D crystals with 3D auxetic properties, which will bring us more breakthroughs in materials with novel Poisson's ratio materials.

Conflicts of interest

There are no conflicts of interest to declare.

Acknowledgement

This work was financially supported in China by the National Natural Science Foundation of China (Nos. 11464032, 11828401, 21103224) and the Startup Project of Inner Mongolia University (21200-5175101), and in USA by NSF-CREST Center

View Article Online
DOI: 10.1039/C9NR07263B

for Innovation, Research and Education in Environmental Nanotechnology (CIRE2N) (Grant Number HRD-1736093). Most computations were carried out in PARATEAR at Guangzhou Supercomputer Center, and part of this research used resources of the High Performance of Computational facility (HPCf), University of Puerto Rico, which is partially supported by an Institutional Development Award (IDeA) INBRE Grant Number P20GM103475 from the National Institute of General Medical Sciences (NIGMS), a component of the National Institutes of Health (NIH), and the Bioinformatics Research Core of the INBRE. Its contents are solely the responsibility of the authors and do not necessarily represent the official view of NIH.

References

1 (a) T. Chivers, *Chem. Rev.*, 1985, **85**, 341–365; (b) T. Chivers, World Scientific: Singapore 2005, p334. (c) T. Chivers, Sulfur–Nitrogen Compounds, Encyclopedia of Inorganic and Bioinorganic Chemistry, 2011, John Wiley & Sons, Ltd. DOI: 10.1002/9781119951438.eibc0214.

2 (a) F. X. Powell, *Chem. Phys. Lett.*, 1975, **33**, 393–395. (b) S. Sensarma and A. G. Turner, *Inorg. Chim. Acta*, 1982, **64**, L161–L162. (c) S. R. Kass and C. H. DePuy, *J. Org. Chem.*, 1985, **50**, 2874–2877. (d) C. Wentrup, S. Fischer, A. Maquestiau and R. Flammang, *J. Org. Chem.*, 1986, **51**, 1908–1910. (e) H. Bender, F. Carnovale, J. B. Peel and C. Wentrup, *J. Am. Chem. Soc.*, 1988, **110**, 3458–3461. (f) R. D. Brown, P. S. Elmes and D. McNaughton, *J. Mol. Spectrosc.*, 1990, **140**, 390–400. (g) R. D. Davy and H. F. Schaefer III, *J. Am. Chem. Soc.*, 1991, **113**, 1917–1922. (h) T. Chivers, P. W. Codding and R. T. Oakley, *J. Chem. Soc., Chem. Commun.*, 1981, 584–585.

3 (a) Y. Jung, T. Heine and P. v. R. Schleyer, *J. Am. Chem. Soc.*, 2004, **126**, 3132–3138. (b) F. De Proft, P. W. Folwer, R. W. A. Havenith, P. v. R. Schleyer, G. Van Lier and P. Geerlings, *Chem. Eur. J.*, 2004, **10**, 940–950.

4 P. Hassanzadeh and L. Andrews, *J. Am. Chem. Soc.*, 1992, **114**, 83–91.

5 M. J. Cohen, C. M. Mikulski, A. F. Garito, A. J. Heeger, A. G. MacDiarmid, M.

View Article Online
DOI: 10.1039/C9NR07263B

S. Saran and J. Kleppinger, *J. Am. Chem. Soc.*, 1976, **98**, 3844–3848.

6 R. W. H. Small, A. J. Banister and Z.V. Hauptman, J. *Chem. Soc., Dalton Trans.*, 1981, 2188–2191.

7 B. G. Kumar and K. Muralidharan, *RSC Adv.*, 2014, **4**, 28219–28224.

8 T. Chivers and J. Proctor, *Can. J. Chem.*, 1979, **57**, 1286–1293.

9 M. Boudeulle, *Crystal Structure Commun.*, 1975, **4**, 9–13.

10 R. L. Greene, P. M. Grant and G. B. Street, *Phys. Rev. Lett.*, 1975, **34**, 89–92.

11 D. Li, F. Tian, Y. Lv, S. Wei, D. Duan, B. Liu and T. Cui, *J. Phys. Chem. C*, 2017, **121**, 1515–1520.

12 D. Laniel, M. Bykov, T. Fedotenko, A. V. Ponomareva, I. A. Abrikosov, K. Glazyrin, V. Svitlyk, L. Dubrovinsky and N. Dubrovinskaia, *Inorg. Chem.*, 2019, **58**, 9195–9204.

13 H. Xiao, X. Shi, X. Liao, Y. Zhang and X. Chen, *Phys. Rev. Mater.*, 2018, **2**, 024002.

14 J.-H. Lin, H. Zhang, X.-L. Cheng and Y. Miyamoto, *Phys. Rev. B*, 2016, **94**, 195404.

15 J. P. Perdew, K. Burke and M. Ernzerhof, *Phys. Rev. Lett.*, 1996, **77**, 3865–3868.

16 P. E. Blöchl, *Phys. Rev. B*, 1994, **50**, 17953–17979.

17 G. Kresse and J. Furthmüller, *Phys. Rev. B*, 1996, **54**, 11169–11186.

18 T. Bučko, J. Hafner, S. Lebègue and J. G.Ángyán, *J. Phys. Chem. A*, 2010, **114**, 11814–.

19 H. J. Monkhorst and J. D. Pack, *Phys. Rev. B*, 1976, **13**, 5188–5192.

20 J. Heyd, G. E. Scuseria and M. Ernzerhof, *J. Chem. Phys.*, 2003, **118**, 8207–8215.

21 G. J. Martyna, M. L. Klein and M. E. Tuckerman, *J. Chem. Phys.*, 1992, **97**, 2635–2643.

22 Y. Wang, J. Lv, L. Zhu and Y. Ma, *Phys. Rev. B*, 2010, **82**, 094116.

23 (a) C. Zhang, J. Liu, H. Shen, X.-Z. Li and Q. Sun, *Chem. Mater.*, 2017, **29**, 8588–. (b) Y. Wang and Y. Ding, *J. Mater. Chem. C*, 2018, **6**, 2245–2251.

24 S. Liu, H. Du, G. Li, L. Li, X. Shi and B. Liu, *Phys. Chem. Chem. Phys.*, 2018, **20**, 20615–20621.

25 A. Waterfeld and R. Mews, *Angew. Chem. Int. Ed. Engl.*, 1981, **20**, 1017.

26 B. K. Ackerman, K. K. Andersen, I. Karup-Nielsen, N. B. Peynircioglu and S.

View Article Online
DOI: 10.1039/C9NR07263B

A. Yeager, *J. Org. Chem.*, 1974, **39**, 964–968.

27 (a) K. D. Schmidt, R. Mews and O. Glemser, *Angew. Chem.*, 1976, **15**, 614–615. (b) H. W. Roesky, M. Witt, B. Krebs and H. Korte, *Angew. Chem. Int. Ed. Engl.*, 1979, **18**, 415.

28 N. Kano, Y. Itoh, Y. Watanabe, S. Kusaka and T. Kawashim, *Angew. Chem. Int. Ed.*, 2008, **47**, 9430–9433.

29 F. L. Hirshfeld, *Theoret. Chim. Acta*, 1977, **44**, 129–138.

30 S. C. Abrahams, *Acta Cryst.*, 1996, **B52**, 790–805.

31 B. J. Feng, Z. Ding, S. Meng, Y. Yao, X. He, P. Cheng, L. Chen and K. Wu, *Nano. Lett.*, 2012, **12**, 3507–3511.

32 A. Fleurence, R. Friedlein, T. Ozaki, H. Kawai, Y. Wang and Y. Yamada-Takamura, *Phys. Rev. Lett.*, 2012, **108**, 245501.

33 L. Li, Y. Yu, G. J. Ye, Q. Ge, X. Ou, H. Wu, D. Feng, X. H. Chen and Y. Zhang, *Nat. Nanotechnol.*, 2014, **9**, 372–377.

34 H. Liu, A. T. Neal, Z. Zhu, D. Tomanek and P. D. Ye, *ACS Nano*, 2014, **8**, 4033–4041.

35 S. Cahangirov, M. Topsakal, E. Akturk, H. Sahin and S. Ciraci, *Phys. Rev. Lett.*, 2009, **102**, 236804.

36 R. Fei and L. Yang, *Appl. Phys. Lett.*, 2014, **105**, 083120.

37 M. Springborg, *Int. Rev. Phys. Chem.*, 1993, **12**, 241–303.

38 T. R. Galeev, B. D. Dunnington, J. R. Schmidt and A. I. Boldyrev, *Phys. Chem. Chem. Phys.*, 2013, **15**, 5022–5029.

39 Q. Pang, L. Liu and J. Zhao, *J. Appl. Phys.*, 2017, **122**, 094302.

40 (a) H. Zhang, L. Liu and Z. Zhou, *Phys. Chem. Chem. Phys.*, 2012, **14**, 1286–1292. (b) H. Zhang, L. Liu and Z. Zhou, *RSC Adv.*, 2012, **2**, 9224–9229. (c) H. Zhang, Y. Yang, Z. Zhou, Y. P. Zhao and L. Liu, *J. Phys. Chem. C*, 2014, **118**, 14662–14669. (d) H. Zhang, X. Q. Zuo, H. B. Tang, G. Li and Z. Zhou, *Phys. Chem. Chem. Phys.*, 2015, **17**, 6280–6288. (e) H. Zhang, G. Tang, X. Zuo, H. Tang, Q. Yang and G. Li, *J. Mater. Chem. A*, 2016, **4**, 12913–12920.

41 J. Bardeen and W. Shockley, *Phys. Rev.*, 1950, **80**, 72−80.

42 M.-Q. Long, L. Tang, D. Wang, L. Wang and Z. Shuai, *J. Am. Chem. Soc.*, 2009, **131**, 17728–17729.

View Article Online
DOI: 10.1039/C9NR07263B

43 M. Long, L. Tang, D. Wang, Y. Li and Z. Shuai, *ACS Nano*, 2011, **5**, 2593–2600.

44 S. Bruzzone and G. Fiori, *Appl. Phys. Lett.*, 2011, **99**, 222108.

45 J. Qiao, X. Kong, Z.-X. Hu, F. Yang and W. Ji, *Nat. Commun.*, 2014, **5**, 4475.

46 Y. Cai, G. Zhang and Y. W. Zhang, *J. Am. Chem. Soc.*, 2014, **136**, 6269–6275.

47 X. Zhang, X. Zhao, D. Wu, Y. Jing and Z. Zhou, *Nanoscale*, 2015, **7**, 16020–16025.

48 Y. Jing, X. Zhang, D. H. Wu, X. D. Zhao and Z. Zhou, *J. Phys. Chem. Lett.*, 2015, **6**, 4252–4258.

49 M. Xie, S. Zhang, B. Cai, Y. Huang, Y. Zou, B. Guo, Y. Gu and H. Zeng, *Nano Energy*, 2016, **28**, 433–439.

50 S. Zhang, M. Xie, F. Li, Z. Yan, Y. Li, Z. Chen and H. Zeng, *Angew. Chem. Int. Ed.*, 2016, **55**, 1666−1669.

51 Y. Jing, X. Zhang, D. Wu, X. Zhao and Z. Zhou, *J. Phys. Chem. Lett.*, 2015, **6**, 4252−4258.

52 T. Cheng, H. Lang, Z. Li, Z. Liu and Z. Liu, *Phys. Chem. Chem. Phys.*, 2017, **19**, 23942−23950.

53 H. Lang, S. Zhang and Z. Liu, *Phys. Rev. B*, 2016, **94**, 235306.

54 C. G. Lee, X. D. Wei, J. W. Kysar and J. Hone, *Science*, 2018, **321**, 385–388.

55 X. Li, Q. Zhang and Q. Wang, *Phys. Chem. Chem. Phys.*, 2013, **15**, 7142–7146.

56 Y. Ding and Y. Wang, *J Phys Chem C*, 2013, **117**, 18266–18278.

57 Y. Chen, X. Liao, X. Shi, H. Xiao, Y. Liu and X. Chen, *Phys. Chem. Chem. Phys.*, 2019, **21**, 5916–5924.

58 T. Ohta, A. Bostwick, J. L. McChesney, T. Seyller, K. Horn and E. Rotenberg, *Phys. Rev. Lett.*, 2007, **98**, 206802.

View Article Online
DOI: 10.1039/C9NR07263B

TOC